Controlling the nature of etched Si nanostructures: High versus low load metal-assisted catalytic etching (MACE) of Si powders

Konstantin Tamarov[†], Joseph D. Swanson[‡], Bret A. Unger[‡], Kurt W. Kolasinski[‡], Alexis T. Ernst[§], Mark Aindow[§], Vesa-Pekka Lehto[†] and Joakim Riikonen[†]*

[†]Department of Applied Physics, University of Eastern Finland, Kuopio, Finland

[‡]Department of Chemistry, West Chester University, West Chester, PA, United States

[§]Department of Materials Science and Engineering, Institute of Materials Science, University of Connecticut, Storrs, CT, United States

*KKolasinski@wcupa.edu

Keywords

Metal-assisted catalytic etching, MACE, porous nanoparticles, silicon powders, silicon nanowires, porous silicon

Abstract

Metal-assisted catalytic etching (MACE) involving Ag deposited on Si particles has been reported as a facile method for the production of Si nanowires (Si NWs). We show that the structure of Si particles subjected to MACE changes dramatically in response to changing the loading of the Ag catalyst. The

use of acetic acid as a surfactant and controlled injection of $AgNO_3$(aq) enhanced Ag deposition. The use of acetic acid and controlled injection of H_2O_2 not only facilitated optimization of the etching step, it allowed us to identify a previously unobserved etching regime that we denote as low-load MACE (LL-MACE). Material produced by LL-MACE exhibits dramatically different yield and structural characteristics as compared to conventionally produced material. We demonstrate production of Si NWs as well as mesoporous Si nanoparticles from an inexpensive metallurgical grade Si powder. High loading of Ag (HL-MACE) generates parallel etch track pores created by the correlated motion of Ag nanoparticles. The uniform size distribution (predominantly 70–100 nm) of the Ag nanoparticles is generated dynamically during etching. The walls of these etch track pores are cleaved readily by ultrasonic agitation to form Si NWs. Low loading of Ag (LL-MACE) creates 10–50 nm Ag nanoparticles that etch in an uncorrelated (randomly directed) fashion to generate a bimodal distribution of mesoporosity peaking at ~4 nm and 13–21 nm. The use of a syringe pump to deliver the oxidant (H_2O_2) and Ag^+ is essential for increased product uniformity and yield. Different process temperatures and grades of Si produced significantly different pore size distributions. These results facilitate the production Si NWs and mesoporous nanoparticles with high yield, low cost, and controlled properties that are suitable for applications in, *e.g.*, lithium ion batteries, drug delivery, as well as biomedical imaging and contrast enhancement.

Table of Contents Graphic

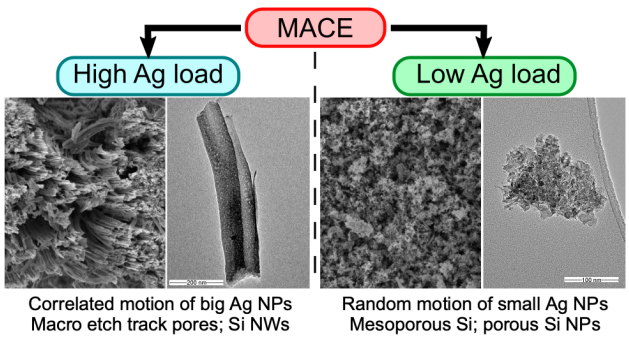

Metal-assisted catalytic etching (MACE) of Si was developed by Peng and co-workers,[1–3] and has been used widely to form Si nanowires (NWs) on Si wafers.[4] Si NWs have found applications in photovoltaics,[5–7] photonics,[8,9], sensing,[10–12] thermoelectric devices[13,14] and anodes of Li-ion batteries.[15–17] Porous[18] and photoluminescent[19] Si NWs as well as Si nanoparticles, have been used for drug delivery[20–22] and biological imaging.[23] Particularly interesting from the standpoint of large-scale applications is that MACE can be used to etch metallurgical grade silicon powder.[24–27]

In MACE, a deposited noble metal catalyzes the reduction of an oxidant, which is accompanied by hole generation in the metal and its injection into Si.[28] The oxidant is most commonly H_2O_2[29,30] but others such as dissolved O_2[31] or V_2O_5[28] have been used. Hole injection induces the dissolution of Si primarily in a valence 2 process accompanied by H_2 production,[28] although other processes, such as tetravalent dissolution of Si and Si oxide formation and dissolution (also a valence 4 process), may also contribute.[32] Since the concentration of holes in Si is maximized near the Si/metal interface, the etching takes place preferentially on the contact area with the metal, rather than on the bare Si surface. However, holes can also diffuse away from the metal/Si interface and induce remote etching.[33] The transport of holes through the Schottky barrier formed at the metal/Si interface depends on the doping level of the Si. Thinning of the space charge region at high doping level enhances tunneling through the barrier.[34] Therefore, porous and photoluminescent Si NWs can be formed with highly doped Si in analogy to galvanic[35] or electrochemical[36] etching. The dissolution by H_2O_2 of deposited Ag followed by its re-deposition may also play a role in remote etching. This process has been demonstrated, for example, by Chiappini *et al*.[20]

Most commonly, Ag is used as the catalyst in MACE, although other noble metals, such as Au, Pd and Pt[37] as well as Ru,[38] Rh[39] and Ni[40] have been reported. MACE may either be performed in a one-step (metal precursor and oxidant combined) or two-step (metal precursor and oxidant in separate solutions) process[1,4,32,41]. The one-step process has been used, for example, to generate low-reflectivity black silicon surfaces for enhancement of solar cell performance.[42,43]

The main challenges in producing Si nanostructures by MACE are the difficulties in controlling the properties of the etch products and the high cost of electronics grade wafers. Using less expensive metallurgical grade Si powders instead of wafers can significantly reduce the costs ($1 vs. $1,000 per kg for electronics grade Si). Few studies have investigated MACE of Si powders. In these studies, high loads of Ag were used to produce material for lithium ion batteries.[25,26] In MACE of Si powders,[27] the Si surface area and Ag amount can be varied significantly without utilizing more sophisticated deposition methods such as sputtering,[44] thermal deposition[4] or lithography.[45]

Here we demonstrate that enhanced control of the nucleation step is obtained by using acetic acid as a surfactant in combination with controlled injection of the metal salt solution. Addition of acetic acid together with controlled injection of the oxidant further optimized the etching step. This allowed us to identify a previously unobserved regime of etching that we denote as low-load MACE or LL-MACE. Material produced by LL-MACE exhibits dramatically different yield and structural characteristics as compared to material produced in conventional MACE.

To identify the low-load regime, we investigated MACE of Si powders and varied the amount of deposited Ag over a wide range, from 4.8 mmol to 0.001 mmol per 1 g of Si powder. Thus, the metal amount to surface area ratio, defined by $\mathrm{MAR} = n(\mathrm{Ag})/A_{\mathrm{Si}}$, varied from 11.4 $\mathrm{mmol \cdot m^{-2}}$ to 0.0024 $\mathrm{mmol \cdot m^{-2}}$ for 44−75 μm Si particles, where $A_{\mathrm{Si}} = 0.42\ \mathrm{m^2\ g^{-1}}$ is the Brunauer-Emmett-Teller (BET) specific surface area. Over this range of MAR values, as shown in the Supporting Information (Section S1.1), the thickness of the Ag layer would be in the range of 118 nm−0.025 nm (288−0.06 atomic layers) assuming a uniform Ag coverage. We categorize MACE into high load (HL-, $n(\mathrm{Ag}) \geq 1$ mmol per g Si, hereafter denoted simply as 1 mmol) and low load (LL-, $n(\mathrm{Ag}) \leq 0.05$ mmol) MACE to distinguish between different morphologies obtained after etching with high and low Ag loadings. The transition region between these limits creates poorly structured material with much lower specific surface area.

Results and Discussion

Effect of Ag load. We began MACE by suspending 1 g of metallurgical grade (99.6 %, MG) 44−75 μm Si powder in acetic acid (10 ml, glacial) and 20 ml hydrofluoric acid (20 ml, 48 %, HF). The desired volume of aqueous $AgNO_3$ solution was then injected using a syringe pump to deposit Ag onto Si surfaces (Section S1.2 of Supporting Information). The use of acetic acid as a surfactant and controlled injection of $AgNO_3$ significantly reduced aggregation of Si particles during deposition. Their use resulted in significantly more facile disaggregation of particles upon commencement of etching. After Ag was deposited, its morphology and particle sizes were examined by SEM and STEM (Figure 1, Section S2.1 of Supporting Information). HL-deposition (Figure 1a−c) led to an extremely heterogeneous Ag layer on the Si particles. Small nanoparticles (15−50 nm) coexisted with larger ones (up to 500 nm) and 3D dendrites that formed on any given Si particle. There was never a continuous film across the whole particle, although some ridges were decorated with an almost continuous layer of Ag (Figure 1a). Etching began *during deposition* in HL samples. Figure 1b and 1c show that the Si surface became highly roughened, and small nanoparticles were found to burrow up to 220 nm below the Si particle surface. These 15−50 nm nanoparticles were approximately spherical, while there were many larger irregular aggregated particles that ranged up to 500 nm (Figure 1c).

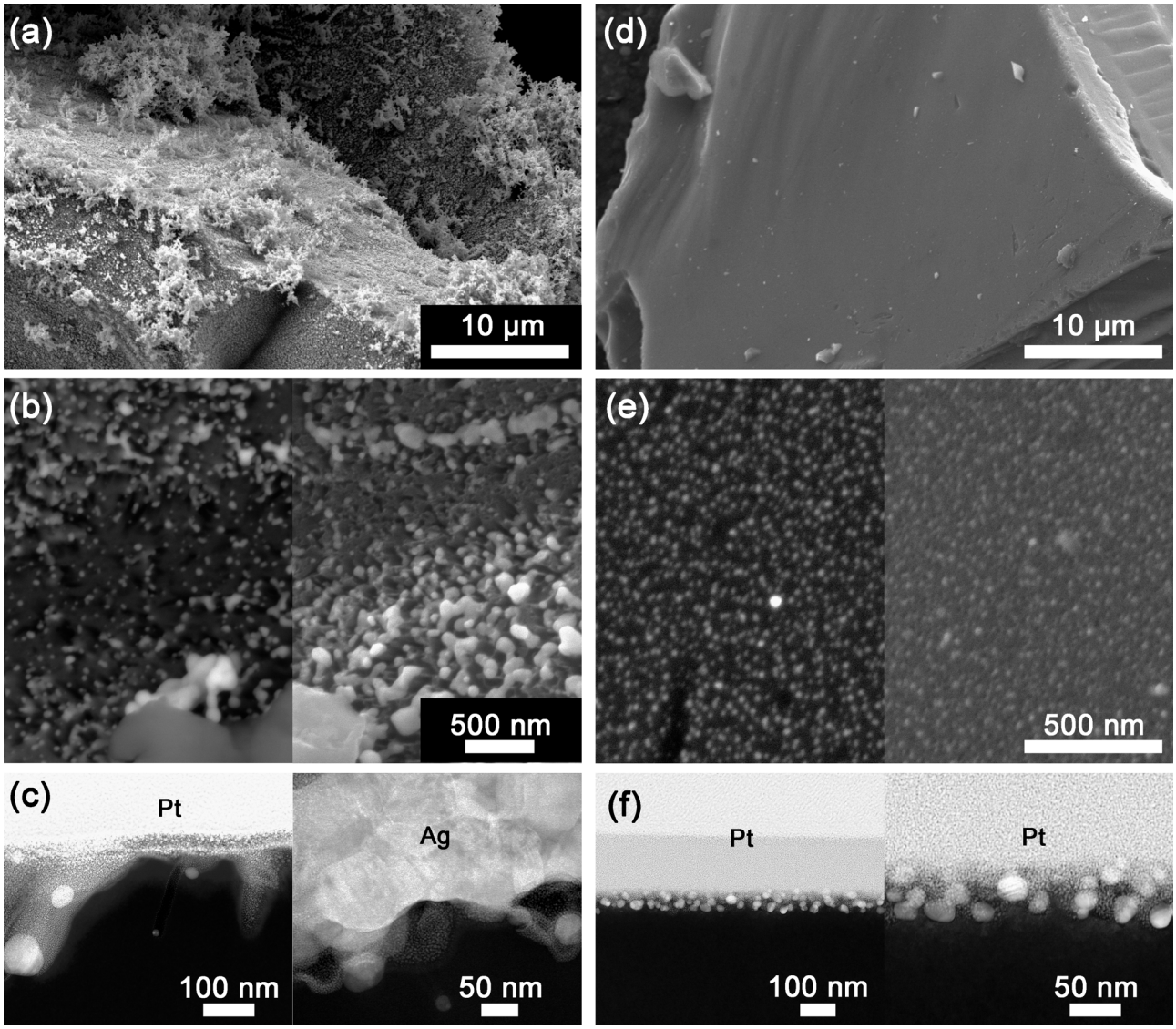

Figure 1. SEM (a,b,d,e) and HAADF STEM (c,f) images of: (a−c) 4.8 mmol of deposited Ag, and (d−f) 0.025 mmol of deposited Ag on the surfaces of MG Si particles. The darker left sides and brighter right sides of (b) and (e) are backscattered and secondary electron images, respectively. The cross-sections in (c) reveal a thick layer of Ag, a roughened Si surface and etch tracks formed during deposition. The cross-sections in (f) reveal small Ag particles confined to the near-surface region. The Pt layers shown in (c) and (f) were used to preserve surface morphology during ion-beam cross sectioning (see EDXS on Figure S2.1, Supporting Information).

The LL-deposition depicted in Figure 1d−f resulted in a random distribution of Ag nanoparticles over virtually the entire Si surface. A narrow Ag particle size distribution with most of the particles

having diameters of 8−20 nm and only a few 30−35 nm particles present (Figure 1e). Cross sections revealed the flatness of the initial Si surface and a similar narrow size distribution of Ag nanoparticles (10−30 nm). Some Ag nanoparticles etched into the Si substrate minimally and were confined to a narrow near-surface region of ~60 nm in depth (Figure 1f) across the imaged lateral region over 5 μm in width.

After Ag deposition, etching was induced by injection of a H_2O_2/H_2O solution at a constant rate with a syringe pump (Section S1.2 of Supporting Information). Solutions contained the specific volume of H_2O_2 required to provide a H_2O_2/Si molar ratio of 0.9. Just as for regenerative electroless etching (ReEtching),[46] the use of a syringe pump was essential to optimize the etching of the powders because they possess much higher surface areas than Si wafers. Controlled H_2O_2 injection maintained steady-state etching, reduced heating, and prevented the process from entering the electropolishing regime caused by excessive H_2O_2 concentration. *H_2O_2 injection allowed us to increase the yield of etched powder from a few percent to over 30 % while still etching the particles all the way through the core* (*vide infra*).

After a 30 min etch, completely different morphologies were obtained in the HL and LL Ag limits. At 4.8 mmol of Ag, Si particles exhibited distinct etch track pores created by cooperative motion among the Ag nanoparticles (Figure 2a-c). The walls of these etch track pores exfoliated to form Si NWs. The cross sections revealed that the Si particles were completely etched through. On the other hand, the LL Ag led to the etching of a mesoporous structure (Figure 2d-f). The porous structure obtained indicates that the pores were formed by uncorrelated motion of the deposited 10−30 nm Ag nanoparticles (Figure 1e).[29,47,48] The porous Si layer was 3−10 μm thick, and the particle core was unetched. As shown below, smaller particles and/or longer etch times were needed to fully porosify the Si particles in the LL limit.

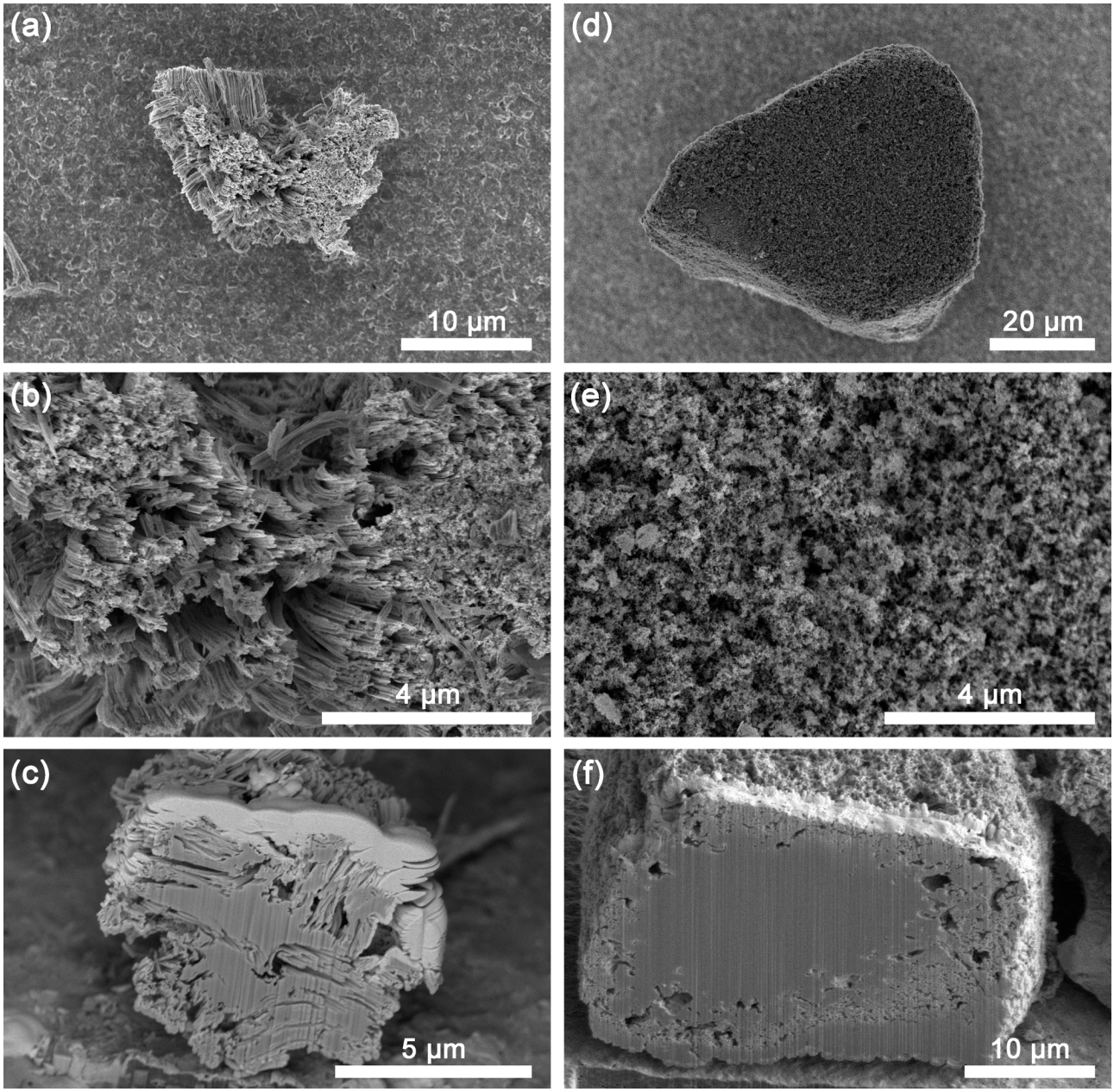

Figure 2. SEM images of MG microparticles after MACE with: (a, b, c) 4.8 mmol of Ag and (d, e, f) 0.025 mmol of Ag. (c) and (f) are cross sections of the microparticles. Pores on (f) are partially filled with Pt, which was used to preserve the porous structure during ion-beam cross sectioning. Si/H_2O_2 molar ratio was 0.9, etching time was 30 min, Ag nucleation time was 40 min and 15 min for high and low Ag loads, respectively.

To identify the differences between HL- and LL-MACE, we examined the morphology of Si and Ag after a 2 min etch (Section S2.1 of Supporting Information). In the HL limit, surface roughness

increased further. Small Ag nanoparticles (15−50 nm on Figure 1c), which descended into Si during the deposition, immediately began to descend further and were found > 800 nm deep (Figure S2.4, Supporting Information). A certain subset of these nanoparticles started to produce 15−30 nm etch track pores. On some Si surfaces, pore tracks formed a forest that looked like incipient Si NWs, while on other surfaces, the tracks formed more connected ridge-like structures. The tips of many Si NWs were decorated with small Ag nanoparticles (Figure S2.2f, Supporting Information), possibly from Ag deposited after the formation of etch track pores. The dendrites and larger particles did not start descending into the Si during the 2 min etch, but instead these features underwent changes in shape and often reorganized into lines (Figure S2.2c, Supporting Information). In the places where this reorganization was observed, Si NW-like structures were formed preferentially. When the lines were not evident, there were more of the ridge-like structures.

As shown in Figure 2 and Supporting Information, after HL-MACE most of Si particles ended up looking similar, with uniform large etch track pores (70−100 nm width, many μm length). *Therefore, after the initial burst of etching by fast small Ag nanoparticles, the Ag deposit dynamically reconfigured to form larger 70−100 nm particles which catalyzed the etching of parallel etch track pores.* The dendrites and large Ag nanoparticles were restructured by a mechanism that was mediated by a substantial amount of dissolved Ag^+, as well as the dissolution and redeposition of Ag to form 70–100 nm nanoparticles that etched Si particles in a coordinated manner. In the HL limit, a significant portion of the Ag remained on the surface of the Si particles.

After 2 min of etching in the LL limit, the Ag nanoparticles were 10−30 nm in diameter, *i.e.* the Ag nanoparticles were small after deposition and remained small after 2 min of etching (Figure S2.3, Supporting Information). Most of the particles were submerged in the Si and etched a fine and randomized mesoporous Si texture with a few larger pits and open mesopores at the exterior surface. *The lack of parallel etch tracks demonstrated that in LL-MACE the motion of Ag nanoparticles was much less correlated compared to the HL limit, and there was much less restructuring of Ag*

nanoparticles, possibly due to the diminished availability of dissolved Ag^+ inside the pores. The etched depth was 250−300 nm after 2 min (Figure S2.4, Supporting Information). The flatness of the original Si surface was mostly intact and not much evidence of surface roughening was observed.

We performed a series of etches with different amounts of Ag to determine the transition point from the formation of uniform etch track pores in the HL limit to the formation of randomized mesoporous Si in the LL limit; we examined the yield, BET surface area, Barrett-Joyner-Halenda (BJH) pore volume (Figure 3), morphology, pore size distributions and crystallite sizes of etched Si particles (Sections S2.2 and S2.3 of Supporting Information). 44−75 μm MG Si particles were etched for 30 min by injecting 6 ml of H_2O_2/H_2O solution to achieve a H_2O_2/Si molar ratio of 0.9. **Figure 4** presents the nitrogen adsorption-desorption isotherms and pore size distributions for four selected concentrations of deposited Ag.

HL-MACE (n(Ag) ≥1 mmol) resulted in the formation of uniform arrays of etch track pores similar to uniform arrays of Si NWs or forest-like structures etched on Si wafers (Figure 2a−c, Section S2.2 of Supporting Information). In this region of deposited Ag amount, most of the Si was removed by the correlated motion of 70−100 nm Ag nanoparticles all the way to the core of the Si particles. The thicknesses of the pore walls did not change significantly along the tracks, and the walls could be cleaved readily to form Si NWs during sonication (Section S2.3 of Supporting Information). At the highest Ag amount (4 and 4.8 mmol) the walls presented some additional mesoporosity (4−20 nm pore width) while for 1−3 mmol of Ag no mesopores were observed (**Figure 4** and Figure S2.7, Supporting Information). Correspondingly, the yield of Si particles without mesopores was slightly higher than for mesoporous ones, and the pore volume was lower (Figure 3a,c). Surface area, however, exhibited the opposite trend and increased slightly with the decrease of Ag amount down to 2 mmol; this could be due to reduced cleavage and/or less etching of wall tips. In the HL regime it has to be recognized that there are two distinct ways in which Si is being etched: the formation of

> 50 nm etch track macropores (to which BJH analysis is not very sensitive) and 2–50 nm mesopore formation (to which BJH analysis is most sensitive).

Decreasing Ag deposition to 0.05 mmol created mesopores exclusively in the < 50 nm region and revealed a drastic decrease in the surface area and pore volume. Si particles etched with 0.5−0.1 mmol deposited Ag presented poor structural characteristics (Figure S2.5, Supporting Information). In this transition region completely unetched Si particles coexisted with partially etched ones. Surfaces of unetched Si particles were only roughened, no deep pores were found. Partially etched particles presented ridge-like structures, substantial unetched parts and almost no mesoporosity. The etch track pores observed on some of the Si particles never reached the particle cores and produced either walls of variable thickness or zig-zag like walls. Thus, the movement of Ag nanoparticles was not well correlated anymore; instead these nanoparticles tended to follow crystallographic directions and possibly changed their sizes and/or shapes during the etching.

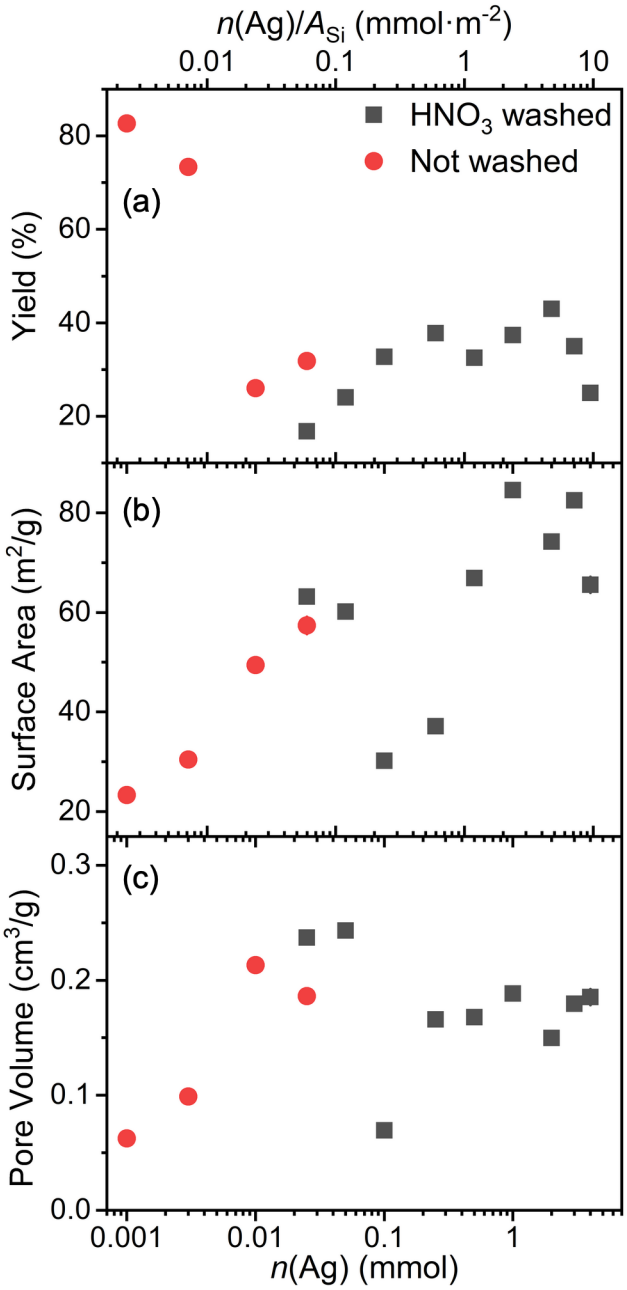

Figure 3. The dependence of yield, BET surface area and pore volume after MACE of 44−75 μm MG Si particles with different amounts of deposited Ag. Samples with $n(\mathrm{Ag}) \geq 0.025$ mmol were subsequently washed with HNO_3 to remove Ag. H_2O_2/Si molar ratio was 0.9, etching time was 30 min, Ag nucleation time was varied to keep the same injection rate of Ag solution.

Further reduction of the Ag amount below 0.1 mmol resulted in the formation of mesoporous Si, which corresponded to a transition at MAR = 0.24 mmol·m^{-2}. LL-MACE etched particles presented a random texture of fine pores, relatively high pore areas and high pore volumes (Figure 3). MG Si

particles after LL-MACE with 0.01−0.05 mmol had high volumes of 3−6 nm pores, while even lower amounts of Ag led to the formation of bimodal pore size distributions (**Figure 4**b and Figure S2.7, Supporting Information). At n(Ag) < 0.01 mmol, a 30 min etch was already not enough to consume all of the injected H_2O_2, and the yield became close to 80 % while the values of surface area and pore volume dropped below 30 $m^2 \cdot g^{-1}$ and 0.1 $cm^3 \cdot g^{-1}$. When the injection time was increased to 3 h for n(Ag) = 0.001 mmol, the volumes of both the 3−6 nm and 9−40 nm pores increased, which led to an increase of surface area up to 55.2 $m^2 \cdot g^{-1}$ and of pore volume up to 0.19 $cm^3 \cdot g^{-1}$ (Figure S2.8, Supporting Information).

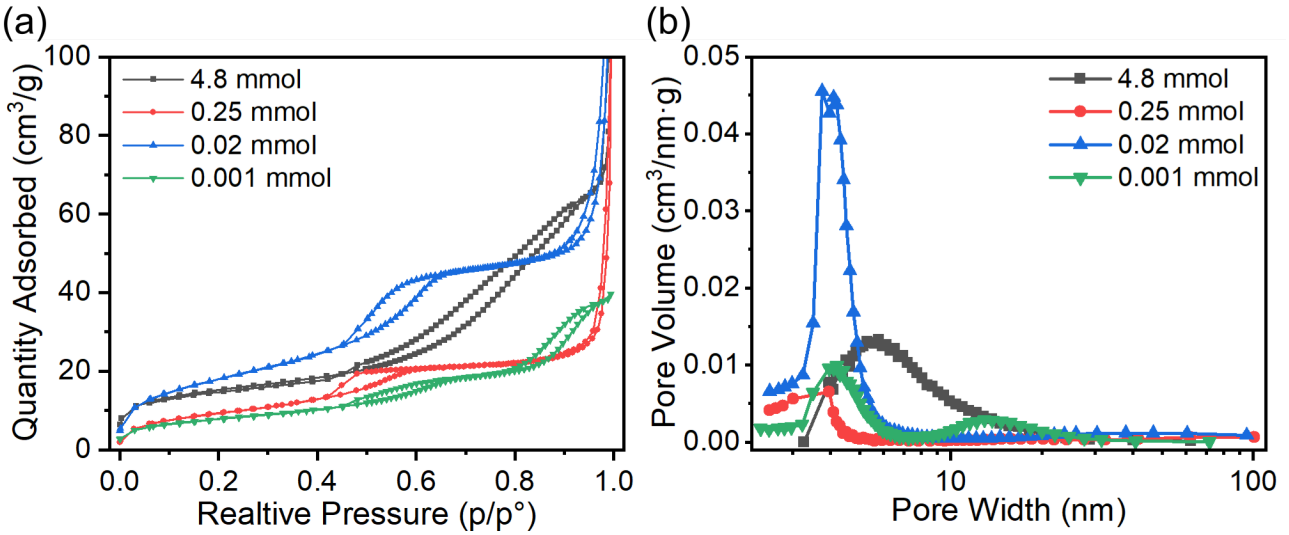

Figure 4. (a) Nitrogen adsorption/desorption isotherm for different amount of deposited Ag; (b) BJH desorption pore size distributions obtained from the isotherms. MG Si particle sizes were 44−75 µm, H_2O_2/Si molar ratio was 0.9, etching time was 30 min, Ag nucleation time was varied to keep the same injection rate of Ag solution.

Si nanostructures formed by MACE could be detached easily from the Si particles by ultrasonic agitation for closer examination with transmission electron microscopy (TEM, Sections S2.9–S2.12 of Supporting Information). TEM imaging confirmed the dramatic differences in the morphologies of the nanostructures. HL-MACE produced Si NWs, while the detached nanostructures after LL-MACE presented irregular shapes and sizes similar to porous Si nanoparticles prepared by fracturing

of electrochemically etched porous Si films.[49,50] The thickness of the Si NWs was in the range of 90–150 nm, which corresponded to the crystallite sizes obtained from X-ray powder diffraction measurements (XRPD, Section S2.13 of Supporting Information). XRPD data additionally revealed the presence of small 5−20 nm crystallites that roughly coincided with the crystallite size estimated from Raman spectra using the phonon confinement model.[51] These small crystallites were found after HL-MACE and LL-MACE and were not present in the transition region of Ag amount, which again highlights the different nature of Si etched in the transition region.

There are several other parameters besides the Ag amount that affect the outcome of the etching. These include: H_2O_2/Si molar ratio, etching time (*i.e.* rate of H_2O_2 solution injection), Si purity and doping, temperature of the etchant, and type of metal catalyst. For example, higher temperatures were shown to increase the rate of Si NWs etching on wafers[52] and the level of doping in Si wafers affected the porosity of the Si NWs.[53,54]

HL-MACE: effect of H_2O_2 amount and etching time. For HL-MACE of 44–75 μm MG Si powders (n(Ag) = 4.8 mmol), we investigated the dependence of H_2O_2/Si molar ratio and etching time (Sections S3 and S4 of Supporting Information, respectively). The yield after a 30 min etch varied linearly with the H_2O_2/Si molar ratio, which is consistent with the H_2O_2 being consumed fully during the reaction to remove Si under the Ag nanoparticles. Increasing the amount of H_2O_2 thus etched out more Si and produced deeper etch track pores. The intercept yield value was 65 %, which is much lower than the ideal value of 100 % for H_2O_2/Si = 0 indicating the presence of additional etching from side reactions. Because such a reduced intercept is not found in the LL regime (*vide infra*), the reduced intercept for HL-MACE must be indicative of some aspect that is specific to the HL-MACE process. Much of this difference results from etching during Ag deposition (~15 % assuming a stoichiometry of two equivalents of oxidant to remove one equivalent of Si).[55] The remaining 20 % must be related to side reactions, for example, driven by nitrate decomposition products, dissolved O_2 and/or light, induced by the heavy coating of Ag. Use of AgF or Ag acetate

would reduce the effects of nitrate addition. The effects of dissolved O_2 and illumination can be excluded by continuous N_2 sparging and performing the reaction in the dark. For all H_2O_2/Si ratios, the pore walls of the etch track pores contained mesopores; the surface area and pore volume increased slowly with the increase of H_2O_2/Si up to 0.9 and then jumped 2.5 times higher at H_2O_2/Si = 1.0 (Figure S3.1, Supporting Information). This jump is related to the excess of H_2O_2 during etching, which could induce more active dissolution of Ag nanoparticles and promote the remote etching of mesopores.[33]

To understand the influence of H_2O_2 concentration per unit time in HL-MACE, we fixed the H_2O_2/Si molar ratio to 0.9 and varied the injection time of the H_2O_2 solution from 10 to 75 min (Section S4 of Supporting Information). At the shortest etching times, 10 and 15 min, etched Si particles presented large parts of surface regions without etch track pores. The walls of the etch track pores were either cleaved during the etching or were completely etched out. One explanation for the lack of etch track pores at such short injection times is that the correspondingly high H_2O_2 concentration drives the system into the electropolishing regime. This effect would be enhanced by the increased temperature associated with the increased reaction rate.

As mention above, in the HL regime Si was etched to form > 50 nm etch track macropores and 2–50 nm mesopores. No clear patterns were found between the etching time and the yield, surface area and pore volume because of the complexity of the pore structure, the presence of side reactions and the difficulty of the nitrogen adsorption method to characterize macropores that are > 50 nm. An etching time of 25 min was found to produce the highest values of surface area and pore volume while keeping the yield close to 25 %. Thus, the optimal parameters to obtain high surface area and porosity are to inject 1.2–1.3 mmol min^{-1} of H_2O_2 at a molar ratio of 0.9 when 1 g of Si powder is etched.

LL-MACE: effect of H_2O_2 amount and etching time. The time-dependence of LL-MACE revealed negligible variability in the properties of the etched particles for etch durations of 30–120 min (Section S5 of Supporting Information). At 30 min, etched Si particles had slightly lower yield

and higher pore volume than other samples, which was attributed to the stronger heating of the etching solution caused by such rapid injection. To reduce heating and obtain more complete etching of the core, all further LL-MACE was performed using 90 min injections of H_2O_2 solution.

The dependence of LL-MACE (n(Ag) = 0.025 mmol) on the H_2O_2 amount was studied with 90 min etch times and 2–44 μm MG Si particles (Section S6 of Supporting Information). The use of smaller size particles was necessary for complete etching, since bigger Si particles still had solid cores (Figure 2). The yield was found to decrease linearly with the increase of H_2O_2/Si molar ratio, and the intercept was 97 ± 4 %, corresponding to the ideal value within experimental uncertainty. This indicates that side reactions, filtration or other losses were negligible. Specific surface area and pore volume increased linearly with H_2O_2/Si molar ratios. Pore volume growth was consistent with the decrease of yield. Pore size distributions contained two distinct pore sizes: 3−7 nm and 10−60 nm, similar to the case of n(Ag) ≤ 0.01 mmol for 44−75 μm Si powder. The Si crystallite size decreased with the increase of H_2O_2/Si molar ratio and small crystallites of ~ 5 nm appeared when the H_2O_2/Si ratio was 0.6 or higher, corresponding to an increase in the number of both 3−7 nm and 10−60 nm pores (Figure S6.2, Supporting Information). SEM imaging revealed the smoothening of the particle edges with the increase of H_2O_2/Si molar ratio (Figure S6.3, Supporting Information), however this did not result in a significant decrease in the particle sizes as no particles passed through the filter during washing.

In contrast to the H_2O_2 dependence at the HL limit, at the LL limit both yield and pore volume had consistent intercept values close to 100 % and 0 $cm^3\ g^{-1}$, respectively. Thus, it can be concluded, that *while in HL-MACE both large etch track pores and mesopores were formed and there was a variety of side reactions, in LL-MACE, all of the injected H_2O_2 was consumed for etching of mesopores.* The bimodal mesopore distribution in LL-MACE resulted from two distinct types of mesopore formation in the absence of side reactions. One type was the formation of meandering 10−50 nm etch track mesopores as observed directly in STEM images (Figure S2.4, Supporting Information). The second type bears a strong resemblance to the ~4 nm mesopores formed in ReEtching.[46] The valence band

holes responsible for this ReEtching process were generated either directly from Ag^+ reduction at the etchant/Si interface or escaped from beneath Ag metal nanoparticles after reduction of H_2O_2 or Ag^+ on the surface of the metal nanoparticle. Although this explanation is rather speculative, we note that almost all of the Ag nanoparticles formed during LL deposition penetrated into the Si particles, whereas a significant amount of the Ag deposited into the dendritic structures during HL deposition remained on the surface. These surface-bound structures might be responsible for a portion of the side reactions, for example, with dissolved O_2 or light, that caused the deviation from ideal intercepts for HL-MACE.

LL-MACE of different Si grades. Similar to the influence of Si wafer resistivity on the porosity of Si NWs,[53,54] the grade and resistivity of the Si particles had a significant effect on the outcome of LL-MACE (Section S7 of Supporting Information). In the pore size distribution, the peak centered about 4 nm was only observed in samples where 99.6 % MG Si, low resistivity reclaimed Si powder and powder from a p+ wafer were used for etching. More pure 99.999 % MG powders and powder from undoped wafer presented only a broad peak covering 8–30 nm pores, equal to the sizes of the deposited Ag nanoparticles (Figure 1). Some of the surfaces of the particles from undoped wafers were not etched at all. *The disappearance of smaller pore sizes for higher purity Si powders is further evidence for the existence of two distinct etching processes.* Etch track pore formation occurs regardless of doping level and leads to larger mesopores. This is the result of Ag nanoparticles of roughly 8–30 nm that deposit on the Si surface. Thereafter, these nanoparticles progress along random and uncorrelated paths to form 8–30 nm etch track pores. This mechanism is analogous to etch track pore formation in HL-MACE; however, the small particle size and/or lower density of Ag nanoparticles present in LL-MACE results in random uncorrelated etch track pores, rather than the highly correlated parallel etch track pores resulting from HL-MACE. A change in the directionality of etching with decreasing metal nanoparticle size is consistent with a model presented elsewhere to explain the crystallographic dependence of MACE.[27] As noted above, the mechanism resulting in the

etching of smaller pores is less clear. This process correlates with the level of impurity and/or doping, and it is induced by some combination of the etching of impurities, remote etching from holes that diffuse away from the Ag/Si interface, and etching initiated by adsorption of Ag^+ ions that do not coalesce into nanoparticles.

Temperature dependence of LL-MACE. The process temperature influenced the outcome of LL-MACE as well (Figure 5, Section S8 of Supporting Information). Etching was performed using an ice bath and water baths at 18 °C and 30 °C as heat sinks, which corresponded to the etching solution temperatures of 16 °C, 30 °C and 52.5 °C, respectively. With the increase of process temperature, the yield decreased, while the surface area increased slightly (Figure 5a). The pore volume did not increase for a change in process temperature from 16 °C to 30 °C, but was significantly higher at the highest temperature of 52.5 °C. The absence of a change in pore volume between 16 °C and 30 °C was accompanied by a noticeable decrease in the volume of the 8–50 nm pores and an increase in both the volume and average size of the 2–7 nm pores (Figure 5b, Table S8.1 of Supporting Information). Increasing the temperature to 52.5 °C led to a further increase in the volume and average size of the 2–7 nm pores. However, the average size and volume of the 8–50 nm pores also increased, resulting in a lower yield. Thus, the process temperature of 30 °C was optimal to reduce the volume of large pores and increase the volume and average size of small pores while keeping the yield relatively high. This temperature prevented the aggregation of Ag to form bigger particles and improved the etching of small pores.

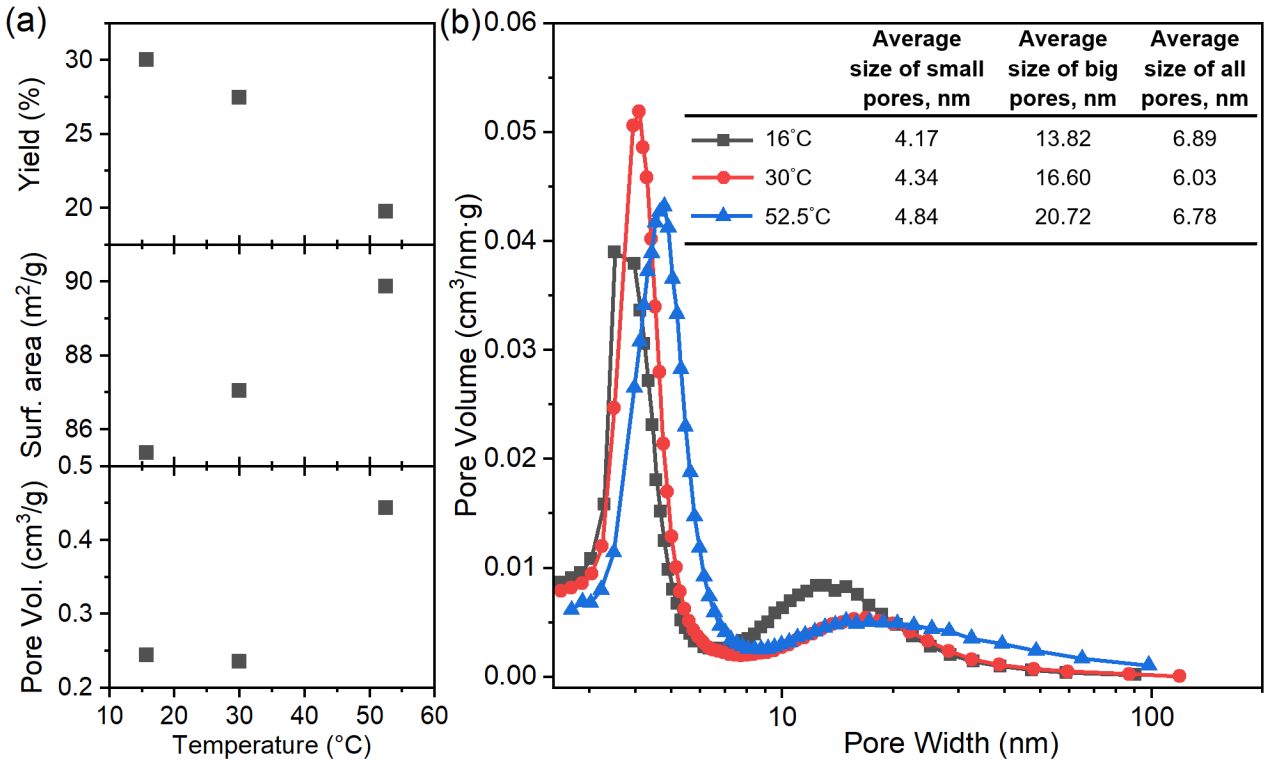

Figure 5. (a) Temperature dependence of yield, BET surface area and pore volume of 11−25 μm MG Si powders after LL-MACE. (b) BJH pore size distributions for the etched powders and average sizes of small pores (peak below 8 nm), average sizes of large pores (peak above 8 nm), and average size of all pores. The amount of deposited metal was 0.025 mmol, nucleation time was 20 min, H_2O_2/Si molar ratio was 0.9 and etching time was 90 min.

Conclusions

In previous studies, porous silicon produced by MACE suffered from poor yield and difficulty in controlling the nanostructure of the products. One order of magnitude improvement in yield and significant improvement in uniformity of the etch products was achieved here by controlled injection of Ag^+ during deposition and H_2O_2 during etching. The improved uniformity combined with pore structure analysis by nitrogen adsorption made it possible to reveal two distinct etching regimes depending on the amount of Ag used. As the amount of deposited Ag was reduced, the morphology of etched particles changed from predominantly parallel etch track pores at high load (high-load

MACE or HL-MACE), to a transition region of poor morphological quality, and finally to a new regime with smaller mesopores accompanied by random etch track pores (low-load MACE or LL-MACE). The distinct mechanistic and structural differences between HL and LL-MACE are highlighted in Figure 6.

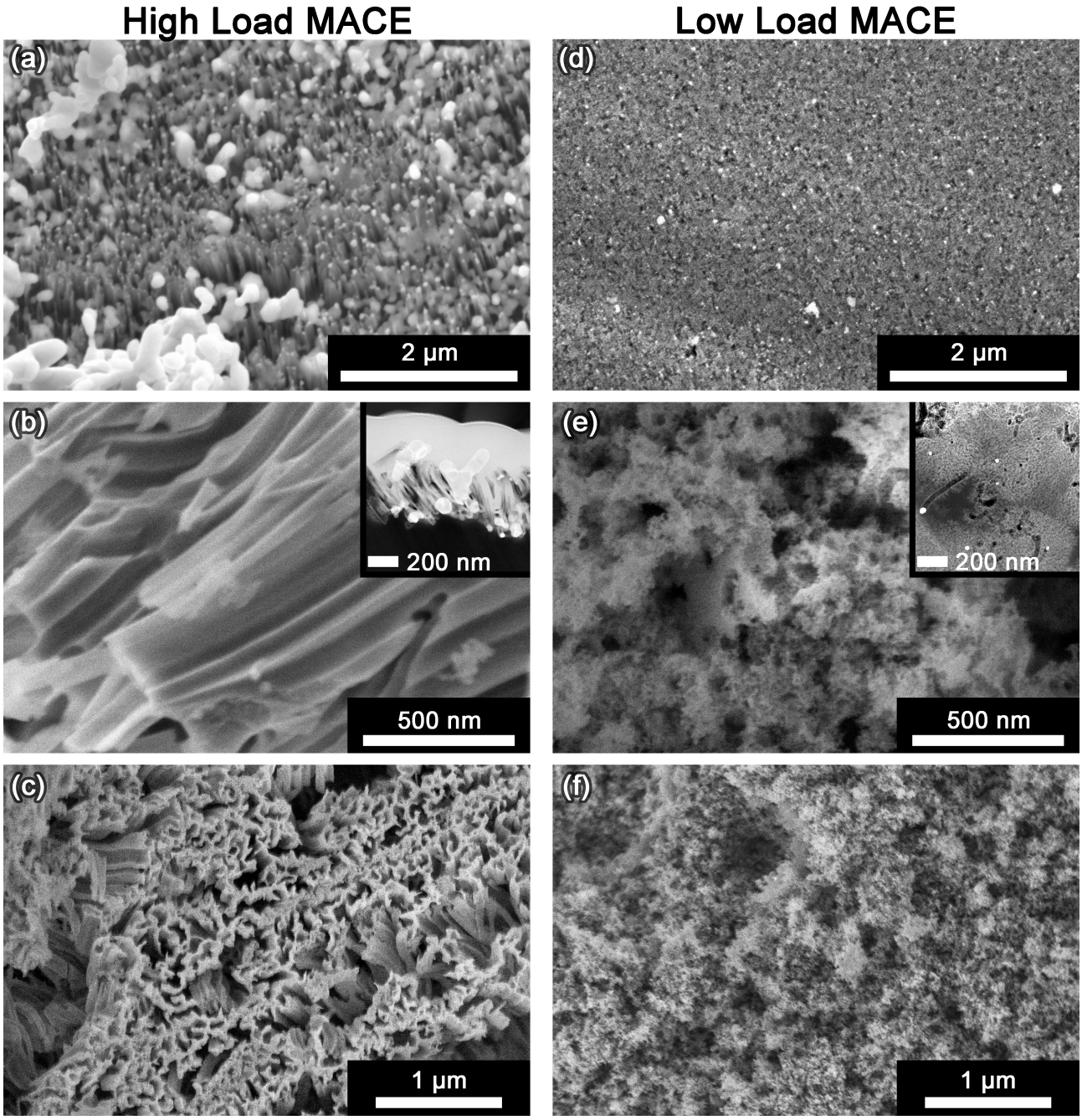

Figure 6. High-load MACE (left-hand column) is characterized by (a) deposition of a thick metal layer composed of dendrites as well as nanoscale and microscale metal particles (plan view); (b) etching that proceeds with correlated motion of the metal nanoparticles to form predominantly 70–

100 nm parallel etch track pores (cross section); and (c) production of etched silicon particles that are rough in texture and covered with ridges formed by the etch track pores (plan view). Low-load MACE (right-hand column) is characterized by (d) light deposition of dispersed individual metal nanoparticles (plan view); (e) uncorrelated etching of random 10–50 nm etch track pores that are surrounded by remotely etched 3–6 nm tortuous pores (cross section); and (f) production of etched particles that are relatively smooth in texture with randomized pores (plan view).

In both HL-MACE and LL-MACE, there were two ways to remove Si: etch track pore formation and remote etching. The propensity for etch track pore formation compared to remote etching was related to the doping level and the amount of deposited Ag. In the HL limit, the primary means of Si removal was etch track pore formation. Due to the high density and large size of the Ag nanoparticles, etch track pores formed by > 50 nm Ag nanoparticles were parallel to one another as a result of correlated Ag nanoparticle motion during etching. With high Ag loading from $AgNO_3$, some Ag remained on the surface of the Si particles resulting in side reactions that wasted Si. In LL-MACE all etching was channeled into mesopore formation and there were no side reactions. Again, etching localized to the vicinity of Ag nanoparticles and remote from them was observed. However, in LL-MACE the smaller Ag nanoparticle size combined with lower density leads to uncorrelated etching and random pore directions.

To conclude, we demonstrated that Si powders can be etched just like Si wafers by MACE to form etch track pores. Stand-alone Si NWs and mesoporous Si nanoparticles can be obtained by sonicating the etched particles. The use of (either electronics or metallurgical grade) Si powders instead of Si wafers offers greater versatility, lower cost and easy scalability. Furthermore, MACE is compatible with regenerative electroless etching[46] (ReEtching) which can be applied after MACE to introduce photoluminescence into nanostructures for, *e.g.*, bioimaging applications.

Methods

Metal-assisted catalytic etching. MACE of Si powders was performed with reagents from different sources, e.g., $AgNO_3$ (Fisher ACS reagent, Alfa Aesar 99.9+ %), HF (Acros Organics 49%, Merck empula® 38−40%), H_2O_2 (Acros Organics 35 % wt.), HNO_3 (Fisher ACS reagent, 65 %, Merck emsure®) and glacial acetic acid (Fisher ACS reagent, Merck, VWR Chemicals). The Si powders were produced by milling metallurgical grade Si particles (Elkem, 99.6 % and 99.999 % purity, polycrystalline), electronics grade wafer chunks (Union Carbide), p+ and undoped Si wafers of resistivities 10–20 mΩ cm and > 100 Ω cm (single crystal, Okmetic). Particle sizes in the powders were 2–44 μm, 44–75 μm, 11−25 μm and 2–10 μm. Distilled and/or deionized water was used in all experiments.

For a typical etch, 1.005 g (±0.005 g) or 0.036 mol of Si powder was first weighted in a PTFE cup. Then, 10 ml of acetic acid was added to the powder and the suspension was sonicated to break the particle aggregates formed after drying. Next, 20 ml of HF was added to the particles and the suspension was stirred in the ice bath until equilibration was reached (no bubbles evolving, etc.). After that, different volumes of 0.6 M or 0.006 M $AgNO_3$ water solution were injected using a syringe pump at rates of 0.17 ml/min or 0.28 ml/min, respectively. During the injection, particles were stirred using a magnetic stirrer. After the $AgNO_3$ injection was finished, particles were further stirred for 5 min to complete the Ag deposition.

The final step was the injection of H_2O_2 solution. The volume of 35% H_2O_2 was calculated based on the value of H_2O_2/Si molar ratio, which was subsequently diluted with water to have the total volume of 6 ml. The H_2O_2 injection time was 30 min for the Ag concentration dependence and was increased to 90 min for further studies at low Ag load to avoid excess heating. During the H_2O_2 injection, particle suspension was stirred and the tube from the syringe was immersed into the Si particle suspension to provide a steady supply of the oxidant. After completion of the etch process, washing with nitric acid of samples with $n(Ag) \geq 0.025$ mmol was performed to remove Ag.

Finally, Si particles were filtered from the suspension using a Büchner style funnel. The appropriate filter was selected to retain the particles. While in the filter funnel, the particles were rinsed with water, then pentane. The sample was then either dried at 55 °C in an oven or at ~40 °C in a vacuum oven. The detailed experimental procedure can be found in Section S1.2 of Supporting Information.

Electron microscopy. For SEM examination, Si powder samples were deposited onto carbon tape and mounted onto Al SEM stubs for direct examination of the surface morphologies using an FEI Quant 400 SEM, a Zeiss Sigma HD VPSEM or an FEI Verios 460L HRSEM.

The cross-sectional imaging was performed using FEI Helios Nanolab G3 dual-beam Ga^+ focused ion beam (FIB) and FEI Helios Xe^+ plasma FIB (PFIB) instruments. A 1-μm thick Pt layer was deposited onto the surfaces of the Si particles *in situ* to protect the surfaces during ion milling. This deposition was accomplished using the electron beam to crack the organometallic Pt precursor. Selected particles were then sectioned using the focused ion beam, and the cross-sectional morphology was directly examined using the electron beam. During the sectioning process, the accelerating voltage used for the ion column was 30 kV and the ion beam currents were reduced iteratively to minimize beam damage.

TEM imaging of the detached nanostructures was performed using a JEOL JEM-2100F instrument. Prior the measurements, approximately 4 mg of particles were placed into 2 ml Eppendorf tubes containing 1 ml of ethanol. The suspensions were then sonicated for 1 hour in an ultrasound bath and centrifuged at 1000 g to separate the big particle cores. The supernatant was then diluted to produce slightly colored suspensions, which were then used for TEM imaging. 2.5 μl of suspension was dropped onto the 400 mesh holey carbon film (Cu, Agar Scientific) and dried for 15 min under a lamp. Finally, the films were placed in the instrument for the imaging.

Structural characterization. The specific surface area (SSA), total pore volume and pore size distribution of the Si samples were determined with N_2 sorption measurements at –196 °C using a

Micromeritics TriStar II instrument. The SSA was calculated from the adsorption isotherm using BET analysis; pore volumes were obtained from the total adsorbed amount at a relative pressure of 0.97; pore size distributions were calculated from the desorption isotherms using BJH theory with a home-written script.

Raman measurements were performed using a Thermo Scientific™ DXR™2xi Raman Imaging Microscope with 50x objective, 795 nm excitation laser and fine grating (400–1800 cm^{-1}). The power of the laser was 0.2 mW, the scan frequency was 200 Hz and number of scans was 200 to avoid heating. For each sample, a layer of particles was tightly glued on a quarter of SEM carbon tape, which itself was glued to a glass microscope slide. The glass slide with particles was placed into a motorized holder and Raman spectra were acquired. A total of four spectra were taken per sample at four different locations. Before starting the measurements for the samples, the Si peak position was measured for a piece of undoped Si wafer. The peak position of the wafer was then normalized to 520.5 cm^{-1} and the normalization constant was subtracted to obtain the correct peak positions for the samples. The calculation of nanocrystal sizes from the Raman peak position was done using the phonon confinement model.[51]

X-ray powder diffraction measurements were performed using a Bruker D8 Discover instrument with Cu tube. The samples were placed on the zero-background holder and measured for 25–117° two theta range with the step of 0.0057° and time per step of 0.205 s (total time of measurement ~1 hour). The crystallite sizes were then estimated using Rietveld refinement method by fitting the XRPD diffractogram with two Si phases and one Ag phase if not all Ag was washed out in several high load MACE samples (Ag crystallite sizes are not shown). TOPAS® 4.6 software was used to fit the full spectrum, calculate crystallite sizes and errors.

Associated Content

Supporting Information

The following files are available free of charge at http://pubs.acs.org. Supporting_Information_LL-MACE.pdf contains the details of experimental procedure, detailed characterization and additional discussion of HL-MACE and LL-MACE. The document includes SEM and TEM imaging of Si particles, N_2 sorption data, crystallite size analysis using XRPD and Raman spectroscopy.

Corresponding Author

*Kurt W. Kolasinski, KKolasinski@wcupa.edu

Author Contributions

KWK was primarily responsible for the design of etching experiments. KT and JDS performed the etching experiments and SEM characterization following up on preliminary work by BAU. MA designed the high-resolution electron microscopy characterization, which was performed by ATE. KT performed N_2 sorption characterization, crystallite size analysis, combined and analyzed the data, and wrote the first draft. All authors participated in writing and approved the manuscript.

Funding

Funding provided by grants #314552 and #314412 from Academy of Finland and the National Science Foundation award #1825331.

Notes

The authors declare no competing financial interest.

Acknowledgment

The authors acknowledge the assistance of PhD Simo Näkki, who performed the first N_2 sorption measurements and MSc Jimi Rantanen for XRPD guidance. The microscopy studies in this paper were performed using the facilities in the UConn/Thermo Fisher Scientific Center for Advanced

Microscopy and Materials Analysis (CAMMA), Center for Microanalysis and Imaging Research and Training (CMIRT) at West Chester University and SIB Labs, Laboratory of Microscopy at University of Eastern Finland. Silicon was provided by Elkem Silicon Materials and Okmetic.

References

(1) Peng, K.-Q.; Yan, Y.-J.; Gao, S.-P.; Zhu, J. Synthesis of Large-Area Silicon Nanowire Arrays via Self-Assembling Nanoelectrochemistry. *Adv. Mater.* **2002**, *14*, 1164.

(2) Peng, K.; Zhu, J. Simultaneous Gold Deposition and Formation of Silicon Nanowire Arrays. *J. Electroanal. Chem.* **2003**, *558*, 35–39.

(3) Peng, K.; Yan, Y.; Gao, S.; Zhu, J. Dendrite-Assisted Growth of Silicon Nanowires in Electroless Metal Deposition. *Adv. Funct. Mater.* **2003**, *13*, 127–132.

(4) Huang, Z.; Fang, H.; Zhu, J. Fabrication of Silicon Nanowire Arrays with Controlled Diameter, Length, and Density. *Adv. Mater.* **2007**, *19*, 744–748.

(5) Stelzner, T.; Pietsch, M.; Andrä, G.; Falk, F.; Ose, E.; Christiansen, S. Silicon Nanowire-Based Solar Cells. *Nanotechnology* **2008**, *19*, 295203.

(6) Sivakov, V.; Andrä, G.; Gawlik, A.; Berger, A.; Plentz, J.; Falk, F.; Christiansen, S. H. Silicon Nanowire-Based Solar Cells on Glass: Synthesis, Optical Properties, and Cell Parameters. *Nano Lett.* **2009**, *9*, 1549–1554.

(7) Li, X.; Xiao, Y.; Bang, J. H.; Lausch, D.; Meyer, S.; Miclea, P.; Jung, J.; Schweizer, S. L.; Lee, J.; Wehrspohn, R. B. Upgraded Silicon Nanowires by Metal-Assisted Etching of Metallurgical Silicon: A New Route to Nanostructured Solar-Grade Silicon. *Adv. Mater.* **2013**, *25*, 3187–3191.

(8) Agarwal, R.; Lieber, C. M. Semiconductor Nanowires: Optics and Optoelectronics. *Appl. Phys. A* **2006**, *85*, 209–215.

(9) Brönstrup, G.; Jahr, N.; Leiterer, C.; Csáki, A.; Fritzsche, W.; Christiansen, S. Optical Properties of Individual Silicon Nanowires for Photonic Devices. *ACS Nano* **2010**, *4*, 7113–7122.

(10) Han, H.; Kim, J.; Shin, H. S.; Song, J. Y.; Lee, W. Air-Bridged Ohmic Contact on Vertically Aligned Si Nanowire Arrays: Application to Molecule Sensors. *Adv. Mater.* **2012**, *24*, 2284–2288.

(11) Mirzaei, A.; Kang, S. Y.; Choi, S.-W.; Kwon, Y. J.; Choi, M. S.; Bang, J. H.; Kim, S. S.; Kim, H. W. Fabrication and Gas Sensing Properties of Vertically Aligned Si Nanowires. *Appl. Surf. Sci.* **2018**, *427*, 215–226.

(12) Georgobiani, V. A.; Gonchar, K. A.; Zvereva, E. A.; Osminkina, L. A. Porous Silicon Nanowire Arrays for Reversible Optical Gas Sensing. *Phys. status solidi A* **2018**, *215* (1), 1700565.

(13) Boukai, A. I.; Bunimovich, Y.; Tahir-Kheli, J.; Yu, J.-K.; Goddard, W. A.; Heath, J. R. Silicon Nanowires as Efficient Thermoelectric Materials. In *Materials for Sustainable Energy*; Co-Published with Macmillan Publishers Ltd, UK, 2010; pp 116–119.

(14) Hochbaum, A. I.; Chen, R.; Delgado, R. D.; Liang, W.; Garnett, E. C.; Najarian, M.; Majumdar, A.; Yang, P. Enhanced Thermoelectric Performance of Rough Silicon Nanowires. *Nature* **2008**, *451*, 163–167.

(15) Zamfir, M. R.; Nguyen, H. T.; Moyen, E.; Lee, Y. H.; Pribat, D. Silicon Nanowires for Li-Based Battery Anodes: A Review. *J. Mater. Chem. A* **2013**, *1*, 9566.

(16) Baek, S.-H.; Park, J.-S.; Jeong, Y.-M.; Kim, J. H. Facile Synthesis of Ag-Coated Silicon Nanowires as Anode Materials for High-Performance Rechargeable Lithium Battery. *J. Alloys Compd.* **2016**, *660*, 387–391.

(17) Li, X.; Yan, C.; Wang, J.; Graff, A.; Schweizer, S. L.; Sprafke, A.; Schmidt, O. G.; Wehrspohn, R. B. Stable Silicon Anodes for Lithium-Ion Batteries Using Mesoporous Metallurgical Silicon. *Adv. Energy Mater.* **2015**, *5*, 1401556.

(18) Qu, Y.; Zhou, H.; Duan, X. Porous Silicon Nanowires. *Nanoscale* **2011**, *3*, 4060–4068.

(19) Gonchar, K. A.; Osminkina, L. A.; Galkin, R. A.; Gongalsky, M. B.; Marshov, V. S.; Timoshenko, V. Y.; Kulmas, M. N.; Solovyev, V. V.; Kudryavtsev, A. A.; Sivakov, V. A. Growth, Structure and Optical Properties of Silicon Nanowires Formed by Metal-Assisted Chemical Etching. *J. Nanoelectron. Optoelectron.* **2012**, *7*, 602–606.

(20) Chiappini, C.; De Rosa, E.; Martinez, J. O.; Liu, X.; Steele, J.; Stevens, M. M.; Tasciotti, E. Biodegradable Silicon Nanoneedles Delivering Nucleic Acids Intracellularly Induce Localized *in Vivo* Neovascularization. *Nat. Mater.* **2015**, *14*, 532–539.

(21) Shalek, A. K.; Robinson, J. T.; Karp, E. S.; Lee, J. S.; Ahn, D.-R.; Yoon, M.-H.; Sutton, A.; Jorgolli, M.; Gertner, R. S.; Gujral, T. S.; et al. Vertical Silicon Nanowires as a Universal Platform for Delivering Biomolecules into Living Cells. *Proc. Natl. Acad. Sci. U. S. A.* **2010**, *107*, 1870–1875.

(22) Peng, F.; Su, Y.; Wei, X.; Lu, Y.; Zhou, Y.; Zhong, Y.; Lee, S.-T.; He, Y. Silicon-Nanowire-Based Nanocarriers with Ultrahigh Drug-Loading Capacity for *In Vitro* and *In Vivo* Cancer Therapy. *Angew. Chem. Int. Ed. Engl.* **2013**, *52* (5), 1457–1461.

(23) Osminkina, L. A.; Sivakov, V. A.; Mysov, G. A.; Georgobiani, V. A.; Natashina, U. A.; Talkenberg, F.; Solovyev, V. V; Kudryavtsev, A. A.; Timoshenko, V. Y. Nanoparticles

Prepared from Porous Silicon Nanowires for Bio-Imaging and Sonodynamic Therapy. *Nanoscale Res. Lett.* **2014**, *9*, 463.

(24) Ouertani, R.; Hamdi, A.; Amri, C.; Khalifa, M.; Ezzaouia, H. Formation of Silicon Nanowire Packed Films from Metallurgical-Grade Silicon Powder Using a Two-Step Metal-Assisted Chemical Etching Method. *Nanoscale Res. Lett.* **2014**, *9*, 574.

(25) Liu, Y.; Chen, B.; Cao, F.; Chan, H. L. W.; Zhao, X.; Yuan, J. One-Pot Synthesis of Three-Dimensional Silver-Embedded Porous Silicon Micronparticles for Lithium-Ion Batteries. *J. Mater. Chem.* **2011**, *21*, 17083.

(26) Bang, B. M.; Kim, H.; Song, H.-K.; Cho, J.; Park, S. Scalable Approach to Multi-Dimensional Bulk Si Anodes via Metal-Assisted Chemical Etching. *Energy Environ. Sci.* **2011**, *4*, 5013.

(27) Kolasinski, K. W.; Unger, B. A.; Ernst, A. T.; Aindow, M. Crystallographically Determined Etching and Its Relevance to the Metal-Assisted Catalytic Etching (MACE) of Silicon Powders. *Front. Chem.* **2019**, *6*, 651.

(28) Kolasinski, K. W.; Barclay, W. B.; Sun, Y.; Aindow, M. The Stoichiometry of Metal Assisted Etching (MAE) of Si in V_2O_5 + HF and HOOH + HF Solutions. *Electrochim. Acta* **2015**, *158*, 219–228.

(29) Li, X.; Bohn, P. W. Metal-Assisted Chemical Etching in HF/H_2O_2 Produces Porous Silicon. *Appl. Phys. Lett.* **2000**, *77*, 2572–2574.

(30) Tsujino, K.; Matsumura, M. Boring Deep Cylindrical Nanoholes in Silicon Using Silver Nanoparticles as a Catalyst. *Adv. Mater.* **2005**, *17*, 1045–1047.

(31) Yae, S.; Kawamoto, Y.; Tanaka, H.; Fukumuro, N.; Matsuda, H. Formation of Porous Silicon by Metal Particle Enhanced Chemical Etching in HF Solution and Its Application for Efficient

Solar Cells. *Electrochem. commun.* **2003**, *5*, 632–636.

(32) Huang, Z.; Geyer, N.; Werner, P.; de Boor, J.; Gösele, U. Metal-Assisted Chemical Etching of Silicon: A Review. *Adv. Mater.* **2011**, *23*, 285–308.

(33) Kolasinski, K. W. Electron Transfer during Metal-Assisted and Stain Etching of Silicon. *Semicond. Sci. Technol.* **2015**, *31*, 14002.

(34) Rezvani, S. J.; Gunnella, R.; Neilson, D.; Boarino, L.; Croin, L.; Aprile, G.; Fretto, M.; Rizzi, P.; Antonioli, D.; Pinto, N. Effect of Carrier Tunneling on the Structure of Si Nanowires Fabricated by Metal Assisted Etching. *Nanotechnology* **2016**, *27*, 345301.

(35) Kolasinski, K. W. Porous Silicon Formation by Galvanic Etching. In *Handbook of Porous Silicon*, 2nd Ed.; Canham, L. T., Ed. Springer, Cham: Berlin, 2017; pp 1-13.

(36) Loni, A. Porous Silicon Formation by Anodization. In *Handbook of Porous Silicon*, 1st Ed.; Canham, L.T., Ed. Springer, Cham, 2014; pp 11–22.

(37) Huang, Z.; Geyer, N.; Werner, P.; de Boor, J.; Gösele, U. Metal-Assisted Chemical Etching of Silicon: A Review. *Adv. Mater.* **2011**, *23*, 285–308.

(38) Sadakane, D.; Yamakawa, K.; Fukumuro, N.; Yae, S. Catalytic Activity of Ru for Metal-Assisted Etching of Si. *ECS Trans.* **2015**, *69*, 179–184.

(39) Yae, S.; Morii, Y.; Fukumuro, N.; Matsuda, H. Catalytic Activity of Noble Metals for Metal-Assisted Chemical Etching of Silicon. *Nanoscale Res. Lett.* **2012**, *7*, 352.

(40) Stafiniak, A.; Prażmowska, J.; Macherzyński, W.; Paszkiewicz, R. Nanostructuring of Si Substrates by a Metal-Assisted Chemical Etching and Dewetting Process. *RSC Adv.* **2018**, *8*, 31224–31230.

(41) Chartier, C.; Bastide, S.; Lévy-Clément, C. Metal-Assisted Chemical Etching of Silicon in

HF–H_2O_2. *Electrochim. Acta* **2008**, *53*, 5509–5516.

(42) Putra, I. R.; Li, J.-Y.; Chen, C.-Y. 18.78% Hierarchical Black Silicon Solar Cells Achieved with the Balance of Light-Trapping and Interfacial Contact. *Appl. Surf. Sci.* **2019**, *478*, 725–732.

(43) Chen, C.-Y.; Wei, T.-C.; Hsiao, P.-H.; Hung, C.-H. Vanadium Oxide as Transparent Carrier-Selective Layer in Silicon Hybrid Solar Cells Promoting Photovoltaic Performances. *ACS Appl. Energy Mater.* **2019**, *2*, 4873–4881.

(44) Huang, Z.; Zhang, X.; Reiche, M.; Liu, L.; Lee, W.; Shimizu, T.; Senz, S.; Gösele, U. Extended Arrays of Vertically Aligned Sub-10 nm Diameter [100] Si Nanowires by Metal-Assisted Chemical Etching. *Nano Lett.* **2008**, *8*, 3046–3051.

(45) Chang, S.-W.; Chuang, V. P.; Boles, S. T.; Ross, C. A.; Thompson, C. V. Densely Packed Arrays of Ultra-High-Aspect-Ratio Silicon Nanowires Fabricated Using Block-Copolymer Lithography and Metal-Assisted Etching. *Adv. Funct. Mater.* **2009**, *19*, 2495–2500.

(46) Kolasinski, K. W.; Gimbar, N. J.; Yu, H.; Aindow, M.; Mäkilä, E.; Salonen, J. Regenerative Electroless Etching of Silicon. *Angew. Chemie Int. Ed.* **2017**, *56*, 624–627.

(47) Gorostiza, P.; Díaz, R.; Anbu Kulandainathan, M.; Sanz, F.; Ramon Morante, J. Simultaneous Platinum Deposition and Formation of a Photoluminescent Porous Silicon Layer. *J. Electroanal. Chem.* **1999**, *469*, 48–52.

(48) Chattopadhyay, S.; Li, X.; Bohn, P. W. In-Plane Control of Morphology and Tunable Photoluminescence in Porous Silicon Produced by Metal-Assisted Electroless Chemical Etching. *J. Appl. Phys.* **2002**, *91*, 6134–6140.

(49) Park, J.-H.; Gu, L.; von Maltzahn, G.; Ruoslahti, E.; Bhatia, S. N.; Sailor, M. J. Biodegradable

Luminescent Porous Silicon Nanoparticles for *in vivo* Applications. *Nat. Mater.* **2009**, *8*, 331–336.

(50) Näkki, S.; Rytkönen, J.; Nissinen, T.; Florea, C.; Riikonen, J.; Ek, P.; Zhang, H.; Santos, H. A.; Närvänen, A.; Xu, W.; et al. Improved Stability and Biocompatibility of Nanostructured Silicon Drug Carrier for Intravenous Administration. *Acta Biomater.* **2015**, *13*, 207–215.

(51) Paillard, V.; Puech, P.; Laguna, M. A.; Carles, R.; Kohn, B.; Huisken, F. Improved One-Phonon Confinement Model for an Accurate Size Determination of Silicon Nanocrystals. *J. Appl. Phys.* **1999**, *86*, 1921.

(52) Cheng, S. L.; Chung, C. H.; Lee, H. C. A Study of the Synthesis, Characterization, and Kinetics of Vertical Silicon Nanowire Arrays on (001)Si Substrates. *J. Electrochem. Soc.* **2008**, *155*, D711.

(53) Georgobiani, V. A.; Gonchar, K. A.; Osminkina, L. A.; Timoshenko, V. Y. Structural and Photoluminescent Properties of Nanowires Formed by the Metal-Assisted Chemical Etching of Monocrystalline Silicon with Different Doping Level. *Semiconductors* **2015**, *49*, 1025–1029.

(54) Geyer, N.; Wollschläger, N.; Fuhrmann, B.; Tonkikh, A.; Berger, A.; Werner, P.; Jungmann, M.; Krause-Rehberg, R.; Leipner, H. S. Influence of the Doping Level on the Porosity of Silicon Nanowires Prepared by Metal-Assisted Chemical Etching. *Nanotechnology* **2015**, *26*, 245301.

(55) Kolasinski, K. W.; Barclay, W. B. The Stoichiometry of Electroless Silicon Etching in Solutions of V_2O_5 and HF. *Angew. Chemie Int. Ed.* **2013**, *52*, 6731–6734.